Journal of Materials Chemistry A

Impact of Processing Conditions on the Film Formation of Lead-Free Halide Double Perovskite Cs2AgBiBr6

Journal:	*Journal of Materials Chemistry A*
Manuscript ID	TA-ART-01-2022-000763.R1
Article Type:	Paper
Date Submitted by the Author:	23-Mar-2022
Complete List of Authors:	Abdelsamie, Maged; Lawrence Berkeley National Laboratory, Materials Sciences Division Cruse, Kevin; University of California Berkeley; Lawrence Berkeley National Laboratory Tamura, Nobumichi; LBNL, Ceder, Gerbrand; University of California Berkeley, Materials Science and Engineering; Lawrence Berkeley National Laboratory, Materials Science Division Sutter-Fella, Carolin; E O Lawrence Berkeley National Laboratory,

Impact of Processing Conditions on the Film Formation of Lead-Free Halide Double Perovskite $Cs_2AgBiBr_6$

*Maged Abdelsamie[1], Kevin Cruse[1,2], Nobumichi Tamura[3], Gerbrand Ceder[1,2], Carolin M. Sutter-Fella[4]**

[1] Materials Sciences Division, Lawrence Berkeley National Laboratory, Berkeley, CA, USA
[2] Department of Materials Science and Engineering, University of California, Berkeley, CA, USA
[3] Advanced Light Source, Lawrence Berkeley National Laboratory, Berkeley, CA, USA
[4] Molecular Foundry Division, Lawrence Berkeley National Laboratory, Berkeley, CA, USA

***E-mail:** csutterfella@lbl.gov

Abstract:

Lead-Free halide double perovskites with enhanced stability have gained attention as a promising environmentally friendly alternative to lead-based halide perovskites. Amongst different halide double perovskites, $Cs_2AgBiBr_6$ has shown attractive optoelectronic properties and stability, making it a promising candidate for stable high-efficiency optoelectronic devices. Motivated by a data mining effort, we present here the effects of different processing strategies on the microstructure and thin-film formation dynamics of $Cs_2AgBiBr_6$. We apply some of the most successfully used solvent engineering approaches from the halide perovskite research to halide double perovskites, namely antisolvent- and additive-assisted synthesis. Using in situ spectroscopy and diffraction, the film formation of $Cs_2AgBiBr_6$ is investigated during spin coating, and the subsequent post-deposition thermal annealing. Dropping antisolvents during spin coating induces immediate supersaturation and crystallization of the wet film, whereas the time of dropping the antisolvent has implications on the film formation dynamics and the final microstructure. For additive (HBr)-assisted synthesis, we show how the addition of HBr affects colloid formation in solution and thus influences the crystallization pathway during thin-film processing. Finally, HBr additive simplifies synthesis in that it doesn't require solution and substrate preheating to obtain pinhole-free films even with higher thickness.

1. Introduction

As an alternative to typically lead-based halide perovskites with structure ABX_3 (A = CH_3NH_3, $CH(NH_2)_2$, Cs, Rb; B = Pb, Sn, Ge; X = I, Br, Cl), lead-free halide double perovskites have emerged as environmentally friendly candidates for optoelectronic applications.[1–4] They are not only of interest for perovskite solar cells (PSCs) but also for other optoelectronic applications such as photodetectors, X-ray detectors, lasers and light-emitting diodes (LEDs) due to their intrinsic thermodynamic stability, suitable band gaps, small carrier effective masses, and low exciton binding energies.[5–7] These halide double perovskites adapt a crystal lattice with general formula $A_2B^+B'^{3+}X_6$ or $A_2B^{4+}X_6$ (A is a monovalent cation, B^+, B'^{3+}, and B^{4+} are monovalent, trivalent, and tetravalent metal cations, respectively , and X is a halide anion), corresponding to mixed mono- plus trivalent-metal double perovskites or tetravalent-metal vacancy ordered double perovskites, repsectively.[7,8] Amongst different halide double perovskites, $Cs_2AgBiBr_6$ has shown attractive optoelectronic properties and stability, making it a promising candidate for stable high-efficiency optoelectronic devices.[9–14] Although the synthesis of $Cs_2AgBiBr_6$ has been successfully demonstrated via solution processing methods,[9–14] mechanistic insights on the thin film formation process are lacking. Understanding the effects of synthetic parameters on the film formation kinetics and its microstructure are of crucial importance since the film quality significantly influences the device performance.[14]

The processing window for high performance devices is narrow and many experimental parameters make it a time-consuming effort to optimize film quality. A plethora of solution engineering approaches has been successfully developed in the lead-based ABX_3 halide perovskite field to improve film quality, stability, charge carrier transport, and performance.[15] Although solution engineering is essential in making high quality ABX_3 films, only a few of these approaches have been applied and optimized for halide double perovskites. Additive processing for example, is commonly used for lead-based perovskites to tune the microstructure and reduce the processing temperature.[16–19] It has been proposed to control the solubility of precursor solutes, coordinate with solutes, act as sites for heterogeneous nucleation, control the kinetics of crystal growth, form crystallized intermediate phases, and facilitate dissolution of intermediate phases.[18–20] Despite its success, additive processing hasn't been applied to halide

double perovskites (beyond its use as a solvent). A second example and possibly the most successful solution engineering approaches for ABX_3 perovskites was the introduction of antisolvent-assisted synthesis.[21,22] Dropping a nonpolar antisolvent which does not dissolve the perovskite during the spin coating of the precursor film accelerates supersaturation by aiding the solvent removal and reducing precursor solubility in the solvent-antisolvent mixture.[23–26] Despite the great success of solution engineering approaches to ABX_3 perovskites, application and systematic optimization via real time process insights to halide double perovskites is rare as evidenced by a text mining effort presented below.

Here we synthesized $Cs_2BiAgBr_6$ thin films via different solution engineering strategies and used *in situ* absorption spectroscopy and grazing incidence wide angle X-ray scattering (GIWAXS) to obtain a fundamental understanding on the film formation pathways. These complementary *in situ* techniques play a critical role in providing time-resolved information on the evolution of structural and optical properties under various synthetic conditions.[27–29] We use this mechanistic understanding of how processing strategies impact film formation pathways to tailor crystallization and microstructure of $Cs_2BiAgBr_6$.

2. Experimental section

Text mining to extract halide double perovskite synthesis publications: Statistics on the body of synthesized halide double perovskites were extracted through a combination of automated and manual text processing techniques, similar to the methods for text mining discussed in Zhao et al.[4] To facilitate automated text extraction, we leveraged article data from a collection of full-text papers mined by the Ceder Group (with years ranging from 2000-2020) and abstracts from MatScholar (with years ranging from 1900-2018).[30,31] Articles from these databases were filtered through a keyword search for “perovskite(s)”. From these articles, any material entities were extracted using Chemical Named Entity Recognition (CNER).[32] Any material entity which contained a formula was analyzed using Pymatgen.[33] Articles containing material formulae with a character length greater than or equal to 7 and with a halide element whose stoichiometry was equal to 6 (corresponding to the $A_2BB'X_6$ double perovskite structure) were accepted. All accepted articles were inspected manually to determine which articles were related to

experimental syntheses. We used Clarivate Analytics' Web of Science literature search tool to search for articles from 2020-present and to account for any articles missing from either of the databases mentioned above. Any halide double perovskite material synthesized under any method within a given article was recorded.

***$Cs_2AgBiBr_6$ synthesis extraction*:** Halide double perovskite synthesis methods were delineated into four categories: crystal synthesis using (1) a solution or (2) a solid-state route, and thin film synthesis using (3) solution or (4) vapor deposition, similar to the text-mined synthesis breakdown in Zhao et. al.[8] In addition to all of the $Cs_2AgBiBr_6$ synthesis articles extracted through the methods above, all remaining relevant publications were found by querying Clarivate Web of Science for articles containing the topic "$Cs_2AgBiBr_6$". The synthesis method used in each article was determined manually. An article could contain multiple syntheses for the same material.

***$Cs_2AgBiBr_6$ thin film solution-deposition synthesis extraction*:** The yield of publications on $Cs_2AgBiBr_6$ thin film solution-deposition syntheses using the automated techniques above was low (only 4 were extracted from the Ceder group or MatScholar databases), so the details for the 57 thin film syntheses were extracted manually from the text. From each synthesis, we extracted the solvent, coating technique, deposition environment, any antisolvents or additives used, and whether the solution and substrate were baked prior to final annealing.

Film Fabrication: The precursor solution was prepared by dissolving 224.35 mg $BiBr_3$ (≥99%, Sigma Aldrich), 93.9 mg of AgBr (≥99.9%, Alfa Aesar), and 212.81 mg CsBr (≥99.9%, Alfa Aesar) in 1 mL dimethylsulfoxide [DMSO] (anhydrous, 99.9%, Sigma-Aldrich) to form a 0.5 M solution. Glass substrates were cleaned by sonication in acetone, isopropyl alcohol (IPA), and de-ionized (DI) water for 10 mins each, then plasma treatment was applied to the cleaned substrates for 5 mins. After complete dissolution of the precursors at 75 °C, both the solution and the plasma-treated glass substrate were either preheated to 75 °C or coated at room temperature. Spin coating was performed for 75 s at 5000 rpm if not stated differently. For samples prepared with dropping an antisolvent, 200 µm of the antisolvent (IPA) was applied at different times during the spin coating. For additive-assisted synthesis, a small amount of hydrobromic acid (HBr) in aqueous solution (48 wt. % in H_2O, ≥99.99%, Acros Organics) was added to the precursor solution and heated at

75 °C for 10 min. After spin coating, the substrates were subsequently annealed at 285 °C for 5 min. All film preparation steps were performed in inert (N_2) environment.

In situ UV-Vis transmission measurements: Transmission measurements were collected using a fiber coupled Ocean Optics spectrometer (Flame) with an integration time of 0.1 s per spectrum. The equation [$A_\lambda = -\log_{10}(T_\lambda)$] was used to calculate the UV-Vis absorbance (A_λ,) from the transmission spectra (T_λ). The *in situ* UV-Vis transmission measurements during spin coating and thermal annealing were performed using a set-up described in a previous work[34] and a custom-built heating stage[35], respectively. The evolution of the absorbance peak near 439 nm related to $Cs_2AgBiBr_6$ phase was used to probe the film formation dynamics.

In situ synchrotron X-ray diffraction (XRD): Synchrotron diffraction measurements during spin coating and thermal annealing were conducted at beamline 12.3.2 at the Advanced Light Source, Lawrence Berkeley National Laboratory. For diffraction measurements during spin coating, the detector (DECTRIS Pilatus 1 M) was located at 35° with respect to the direct beam and ≈ 226 mm from the sample. For diffraction measurements during thermal annealing, the detector was located at 40° with respect to the direct beam and ≈ 191 mm from the sample. A finely ground Al_2O_3 reference sample was used to calibrate the detector geometry. Measurements were performed at wavelength 1.2398 Å with an incident angle of 1-2°. For diffraction measurements during thermal annealing, the samples were spin-coated in N_2-glove-box then heated to 285 °C at the beamline, with an average rate of 50 °C. s^{-1}, and were held at 285 °C for 5 min. The heating stage used for X-ray diffraction during thermal annealing is an ANTON-PAAR DHS900 stage adapted to fit onto the beamline sample stage. The samples were enclosed inside a N_2-filled dome made of a high-performance polymer (poly(ether- ether-ketone), known as PEEK). The dome was cooled by air flow when the heater reached a temperature of 200 °C.

Scanning electron microscopy (SEM): SEM images were collected using a Quanta FEG 250 instrument at an electron beam acceleration of 10 kV.

Dynamic light scattering (DLS): DLS measurements were performed using a NanoPlus-3 instrument. The measurements were done with a quartz cuvette at 80 ^oC.

Raman spectroscopy: Raman spectra were collected using a confocal Raman microscope (LabRAM HR, Horiba Yvon Jobin) with an excitation wavelength of 532 nm. The typical acquisition time for each spectrum was 10 s.

Spectroscopic ellipsometry: A variable-angle infrared spectroscopic ellipsometer IR-VASE from J.A. Woollam Co. Inc was used to extract the thickness of $Cs_2AgBiBr_6$ films.

3. Results and discussion

3. 1. Data mining of $Cs_2AgBiBr_6$ synthesis recipes

Text-mining was employed to generate an overview of synthesis processes used to fabricate $Cs_2AgBiBr_6$ from the existing literature body. **Figure 1**a illustrates the distribution of synthesized halide double perovskite materials out of 337 experimental publications, with $Cs_2AgBiBr_6$ having the highest share (43%) of experimental publications among halide double perovskites. Apart from $Cs_2AgBiBr_6$, other halide double perovskites have been synthesized, including $Cs_2AgInCl_6$, $Cs_2AgBiCl_6$, Cs_2SnI_6, $Cs_2AgSbCl_6$, $Cs_2NaBiCl_6$, $Cs_2NaInCl_6$, Cs_2SnBr_6, Cs_2SnCl_6, $Cs_2AgInBr_6$, $Rb_2AgInBr_6$, and $Rb_2CuInCl_6$.[36–44] The large share of $Cs_2AgBiBr_6$ in experimental publications is probably due to the ease of processability of $Cs_2AgBiBr_6$ from solutions due to the relatively good solubility of $Cs_2AgBiBr_6$ precursors as compared to other halide double perovskite compounds.[7,8] **Figure 1**b shows the distribution of the most used processing techniques to synthesize $Cs_2AgBiBr_6$ out of 155 experimental publications. Solution synthesis is dominant for both crystal synthesis (54%) and thin film synthesis (38%), whereas thin film vapor deposition and solid-state crystal synthesis have a smaller share (5% and 3%, respectively). In **Figure 1**c-h, we show an overview of synthetic approaches/parameters to fabricate $Cs_2AgBiBr_6$ thin films via solution synthesis, including deposition environment, coating technique, solvent, application of pre-annealing, and the use of antisolvents or additives for a total of 57 $Cs_2AgBiBr_6$ solution-based thin film syntheses from 56 experimental publications. As shown in **Figure 1**c, a wide range of deposition environments have been reported including inert glovebox (either N_2 or Ar or not specified) and ambient atmosphere. Nevertheless, the deposition environment wasn't mentioned in 58% of the publications. Spin coating is by far the most used solution coating technique for $Cs_2AgBiBr_6$ thin films (98% of the publications) whereas drop casting has been used otherwise (**Figure 1**d). Due

to the limited solubility of precursor materials, only few solvents have been used to synthesize $Cs_2AgBiBr_6$ thin films. DMSO is the most common used solvent followed by mixed DMSO and dimethylformamide (DMF), see **Figure 1**e. Pre-annealing (or also called hot-casting) approaches, where both the solution and substrate are pre-heated prior to casting, is widely used to obtain high-quality $Cs_2AgBiBr_6$ thin films. As shown in **Figure 1**f, the pre-annealing approach has been used in 60% of the publications. While antisolvent-processing is the most successful route for lead-based halide perovskites, the majority, 61%, of $Cs_2AgBiBr_6$ solution-based thin film syntheses did not report on any antisolvent treatment. From the remaining 39%, chlorobenzene was the most used followed by isopropanol (**Figure 1**g). Finally, regarding additive-assisted processing, only 4% of reported syntheses have relied on additives such as tetrabutylammonium bromide (TBAB), **Figure 1**h.[45] Other additives previously reported include polymeric additives such as poly(ethylene oxide) (PEO), poly(vinyl alcohol) (PVA), poly(vinylidene fluoride) (PVDF), poly(methyl methacrylate) (PMMA), and poly(2-hydroxyethyl methacrylate) (PHMA).[46] These polymers were used to form micrometers thick composite films consisting of a lead-free halide double perovskite embedded in a polymer matrix for X-ray detector applications.[46]

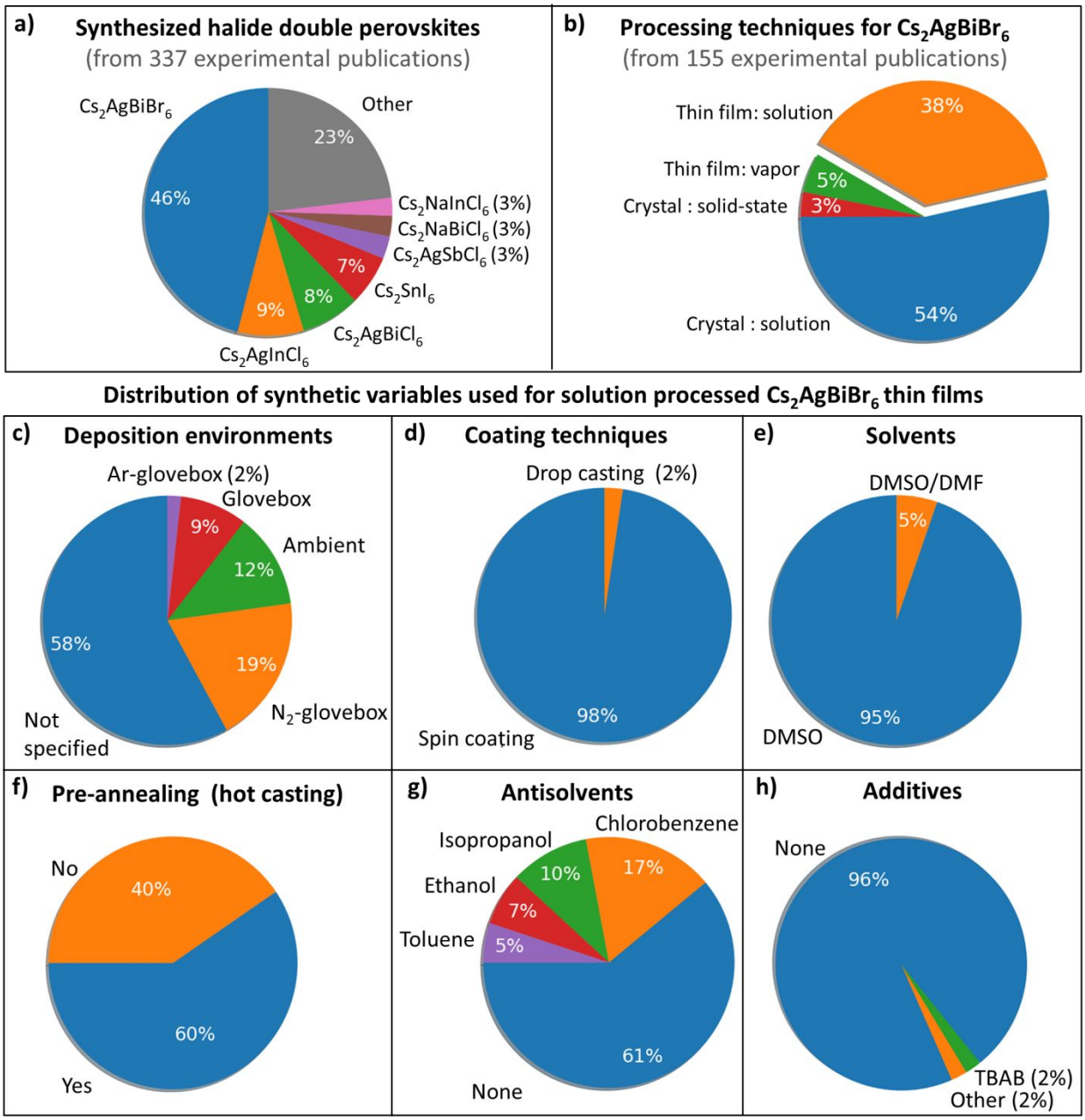

Figure 1 (a, b) Pie-charts of data mining of the distribution of synthesized halide double perovskites from 337 experimental publications and the distribution of processing techniques for $Cs_2AgBiBr_6$ from 155 experimental publications, respectively. (c-h) Detailed distribution of synthetic approaches and parameters used for thin-film solution processing of $Cs_2AgBiBr_6$ from 57 published syntheses (extracted from 56 experimental publications): (c) deposition environments, (d) coating techniques, (e) solvents, (f) the use of pre-annealing (hot-casting), (g) antisolvent treatment, and (h) additive-processing.

3. 2. Effects of solvent engineering on $Cs_2AgBiBr_6$ thin film microstructure

We first show that smooth, pinhole-free and homogeneous microstructures can be obtained by antisolvent dropping and via additives in precursor solutions in contrast to films containing pinholes in the absence of solution engineering. **Figure 2**a-c show scanning electron microscopy (SEM) images of $Cs_2AgBiBr_6$ films when prepared without treatment (reference sample), via antisolvent-treatment, or via additive (HBr)-assisted synthesis. The reference sample appears with pinholes across the film, but pinhole-free films can be obtained by dropping an antisolvent or the addition of HBr to the precursor solution. Integrated scattering intensity from GIWAXS measurements of the annealed films reveal the formation of phase pure $Cs_2AgBiBr_6$ for all three conditions (**Figure 2**d) and confirmed by Raman spectroscopy (**Figure 2**e). The latter shows distinct characteristics of $Cs_2AgBiBr_6$ in the absence of secondary phases such as $Cs_3Bi_2Br_9$ (compare Raman spectra in **Figure S1**a).

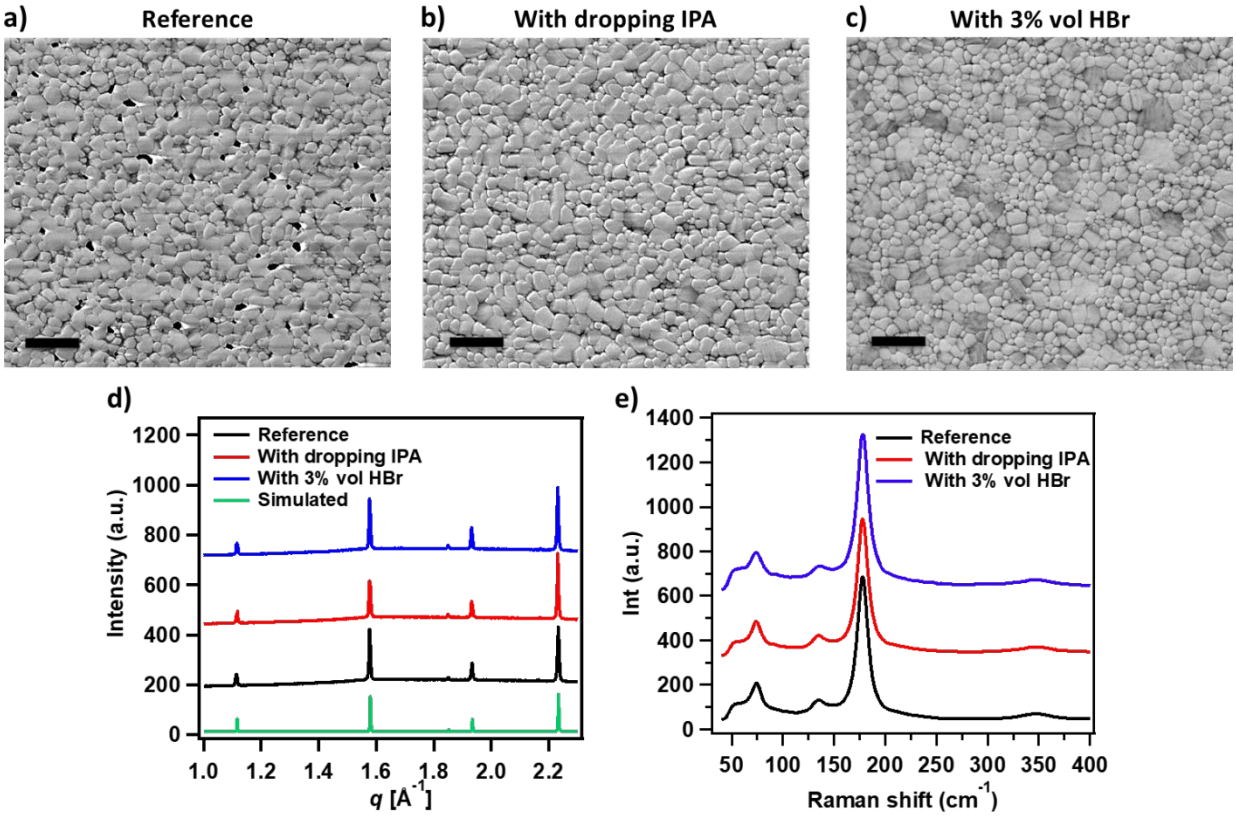

Figure 2 (a-c) SEM images of $Cs_2AgBiBr_6$ thin films; (a) reference sample, (b) prepared with dropping IPA at 12 s from the start of spin coating, and (c) prepared with adding 3% vol HBr to precursor solution. The scale bar for samples in (a-c) is 2 µm. All films in (a-c) were prepared using

hot-casting. (d) Integrated scattering intensity from GIWAXS measurements and (e) Raman spectra of samples shown in (a-c). The simulated diffraction pattern of $Cs_2AgBiBr_6$ is shown in green in (d); calculated using a CIF file from a previous work.[9]

3. 3. In situ UV-Vis absorption during spin coating and thermal annealing

Next, we conducted *in situ* UV-Vis absorption spectroscopy during spin coating and subsequent thermal annealing of $Cs_2AgBiBr_6$ films to investigate the film formation kinetics. The UV-Vis spectra for the reference sample are shown in **Figure 3**. During the initial few seconds of spin coating, we observe a reduction in absorbance of the precursor solution mostly around 400 nm (marked by a violet arrow) which can be explained by loss of precursor materials due to solution spinning off (**Figure 3**a-b). This is followed by a step where no significant changes in absorbance are observed where the solvent evaporates but supersaturation is likely not reached yet, thus crystallization from solutes hasn't started. Upon reaching supersaturation, nucleation and film formation starts signified by a red-shift and an increase in the absorbance peak near 439 nm (marked by a red arrow in **Figure 3**a). It is worth noting that the absorbance peak near ~ 420-440 nm can be due to either $Cs_3Bi_2Br_9$ or $Cs_2AgBiBr_6$ phases. To clarify which of the two phases is present, we performed Raman spectroscopy measurements on the as-cast spin-coated films. Raman spectra support the presence of $Cs_2AgBiBr_6$ phase rather than $Cs_3Bi_2Br_9$ phase in the as-cast films (see **Figure S1b**). Thus, we attribute the absorbance near 439 nm to the $Cs_2AgBiBr_6$ phase. The evolution of the absorbance peak near 439 nm can be used to determine the film formation dynamics during spin coating which dominantly occur from ~ 25 s to ~ 37 s revealed by the gradual increase of the absorbance peak (**Figure S2**a). During the subsequent thermal annealing (**Figure 3**c and **Figure S3**a), the changes in absorption spectra are dominated by a red shift of the absorption edge during the initial 15-20 s, followed by constant characteristics.

It is known from the ABX_3 perovskites that the ideal antisolvent dropping time is crucial and depends on solvent, precursor concentration, spin-speed, as well as subtle variations in deposition environment.[15,47,48] Under ideal conditions, dropping an antisolvent results in pinhole-free films (**Figure 2**b). The SEM images in **Figure 4**a-c reveal that the dripping time has significant effects on the film microstructure. For early dripping times ($\lesssim$ 10 s from the start of the spin coating), the films appear with more and larger pinholes as compared to the reference film. When

the antisolvent is dropped too late (≳ 15 s), the antisolvent treatment is not effective in eliminating pinholes from $Cs_2AgBiBr_6$ films as shown in **Figure 4**b. The optimum dripping time leading to pinhole-free films was found to be ~ 12 s for the given chemistry and synthesis conditions (*i.e.* spin coating 0.5 M solution in DMSO at 5000 rpm) (**Figure 4**c).

In situ absorption measurements during synthesis with antisolvent reveal the effects of different dripping times on film formation dynamics (**Figure 4**d-f). Upon dropping the antisolvent a red shift is observed and a sharp increase in absorbance near 439 nm irrespective of the drop time. As shown in **Figure 4**d, when the antisolvent is dropped early (≲ 10 s), an initial sharp increase in absorbance is followed by a sharp decrease and then a gradual increase in absorbance near 439 nm. These three stages can be explained as dropping IPA induces immediate crystallization, followed by redissolution of the formed crystals due to the high amount of DMSO at this early stage of spin coating, then the crystallization develops gradually with solvent removal.[49] When the antisolvent IPA is dropped too late (≳ 15 s), most of the solvent is ejected and film formation occurs quickly within 2 s (**Figure 4**e). We attribute this behavior to the quick removal of the remaining DMSO by the antisolvent inducing immediate supersaturation and film formation. For films prepared with dropping IPA at the ideal time (~12 s), when reaching the solubility limit and supersaturation, there is a sharp initial increase in absorbance, followed by a gradual increase near 439 nm (**Figure 4**f). Notably, the solutes supersaturate immediately upon exposure to an antisolvent if the antisolvent is dripped at the ideal time as described in previous studies.[24,25] The function of the antisolvent is to wash out the solvent and it initiates supersaturation because solutes are not soluble in the antisolvent. We interpret the initial immediate film formation upon dropping the antisolvent by the quick initial wash out of DMSO and antisolvent-induced supersaturation, while the second film formation step is likely due to slower DMSO removal via evaporation during spinning and exhibits a slower rate (see **Figure 4**f and **Figure S2**a). There is however, also the possible interaction of the antisolvent with the solute which can influence the crystallization. Next, we performed in situ absorption measurements during subsequent thermal annealing (**Figure S3**b). Similarly, to the films prepared without IPA, we observe a red shift in absorption edge during the initial 15-20 s, followed by steady absorption characteristics as shown in **Figure S3**b. While dropping IPA at 12 s was effective to obtain pinhole-

free films, using another antisolvent such as toluene wasn't as effective as IPA and requires its own optimization with respect to dropping time. This behavior was reported previously and IPA was shown to obtain smoother, and pinhole-free films as compared to toluene.[50] It is worth noting that previous studies have investigated various antisolvents with different properties (polarity, boiling point) including IPA, toluene, chlorobenzene, methanol and ethanol, but only IPA was found to form the neat and smooth film without pinholes.[50]

Although the antisolvent treatment helps to obtain pinhole-free $Cs_2AgBiBr_6$ films, there is an optimum processing window which requires optimization for each individual chemistry. Additionally, a combination of hot-casting and antisolvent treatment is required to obtain pinhole-free films.[50] Therefore, we have looked for alternative and simplified processing strategies to obtain pinhole-free films and found that additive-processing using HBr fulfills these criteria (SEM images in **Figure 2**c and **Figure S4**). To reveal the effects of HBr additive on film formation, we have again performed *in situ* UV-Vis absorption measurements during spin coating (**Figure 5**a-b) and the subsequent thermal annealing (**Figure 5**c-d) with 3% vol HBr in solution. *In sit*u UV-Vis absorption measurements during spin coating reveal significant differences not only in the dynamics of the film formation but also in the spectral features for films prepared with HBr (**Figure 5**a-b) as compared to the reference film (**Figure 3**a-b). Evolution of an additional absorbance peak near 410 nm is observed together with the peak near 439 nm (**Figure 5**a-b), suggesting the evolution of a secondary phase during spin coating. **Figure S2**b shows a comparison of absorbance spectra of the as-cast reference film, the film prepared with dropping IPA, and with HBr additive. All spectra exhibit peaks near 439 nm, but the as-cast films prepared with HBr exhibit a second peak near 410 nm. Furthermore, the evolution of the absorbance peak near 439 nm is delayed in the presence of HBr and film formation dominantly occurs from ~ 30 s to ~ 39 s (**Figure S2**a). Since HBr is an aqueous solution (48 wt. % in H_2O), and to exclude the effect of water, we have performed *in situ* UV-vis absorption measurements during spin coating of a $Cs_2AgBiBr_6$ precursor solution with the addition of 3% vol H_2O. It is confirmed that the additional peak near 410 nm is associated with HBr and not with H_2O as visible in **Figure S5** showing only the peak near 439 nm.

It was reported that addition of hydrohalic acids to ABX_3 precursor solutions can alter colloid size and dispersion.[51] To further evaluate the effect of HBr, we have performed dynamic light scattering (DLS) of $Cs_2AgBiBr_6$ precursor solutions without and with the addition of 3% vol HBr, as shown in **Figure S6**. The reference precursor solution exhibits three different colloidal size distributions centered around ~100 nm, ~1.2 µm, and ~75.5 µm. In the presence of HBr, these three colloidal size distributions are shifted to smaller sizes centered around < 50 nm, ~0.3 µm, and ~50 µm. The addition of HBr to the precursor solution not only reduces the colloidal size of species in solution but also leads to a narrower size distribution. Notably, part of the lowest size distribution (i.e. < 50 nm) is outside the feasible measurement range; thus, only a portion of it is measured. These results indicate that HBr increases the solubility of halides in the precursor solution which can explain the delayed film formation during spin coating.

During the subsequent thermal annealing of samples prepared with HBr, we observe growth of the absorbance peak near 439 nm at the expense of absorbance peak near 410 nm, followed by a red shifting of the absorbance edge as shown in **Figure 5**c-d. Upon thermal annealing, the absorbance spectra of films prepared with HBr appear identical to absorbance spectra of the reference film and films prepared with IPA, as shown in **Figure S2**c. We note that the absorption measurements are not particularly sensitive to the presence/absence of a small fraction of pinholes, thus all annealed films exhibited identical absorbance regardless of the clear differences in the microstructure as revealed by SEM images in **Figure 2** and **Figure S4.**

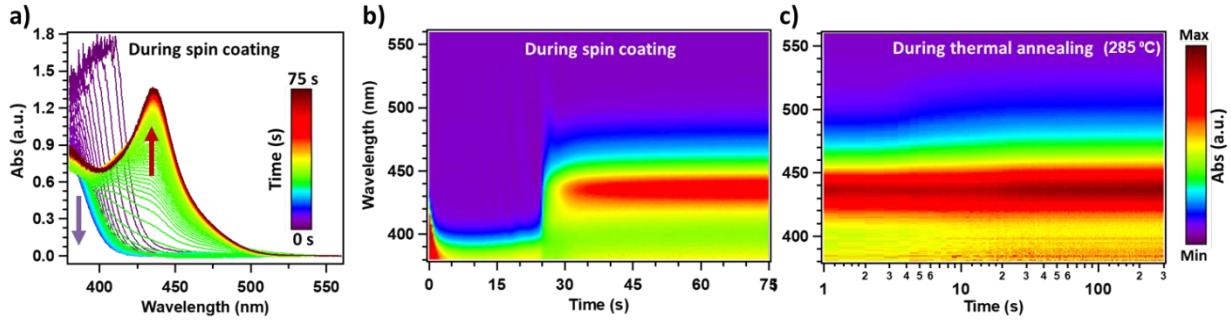

Figure 3 (a) Time-resolved absorbance spectra during spin coating of $Cs_2AgBiBr_6$ precursor solutions. (b-c) 2D color plots of *in situ* absorption measurements: (b) during spin coating of $Cs_2AgBiBr_6$ precursor solution and (c) during the subsequent thermal annealing at 285 ^oC.

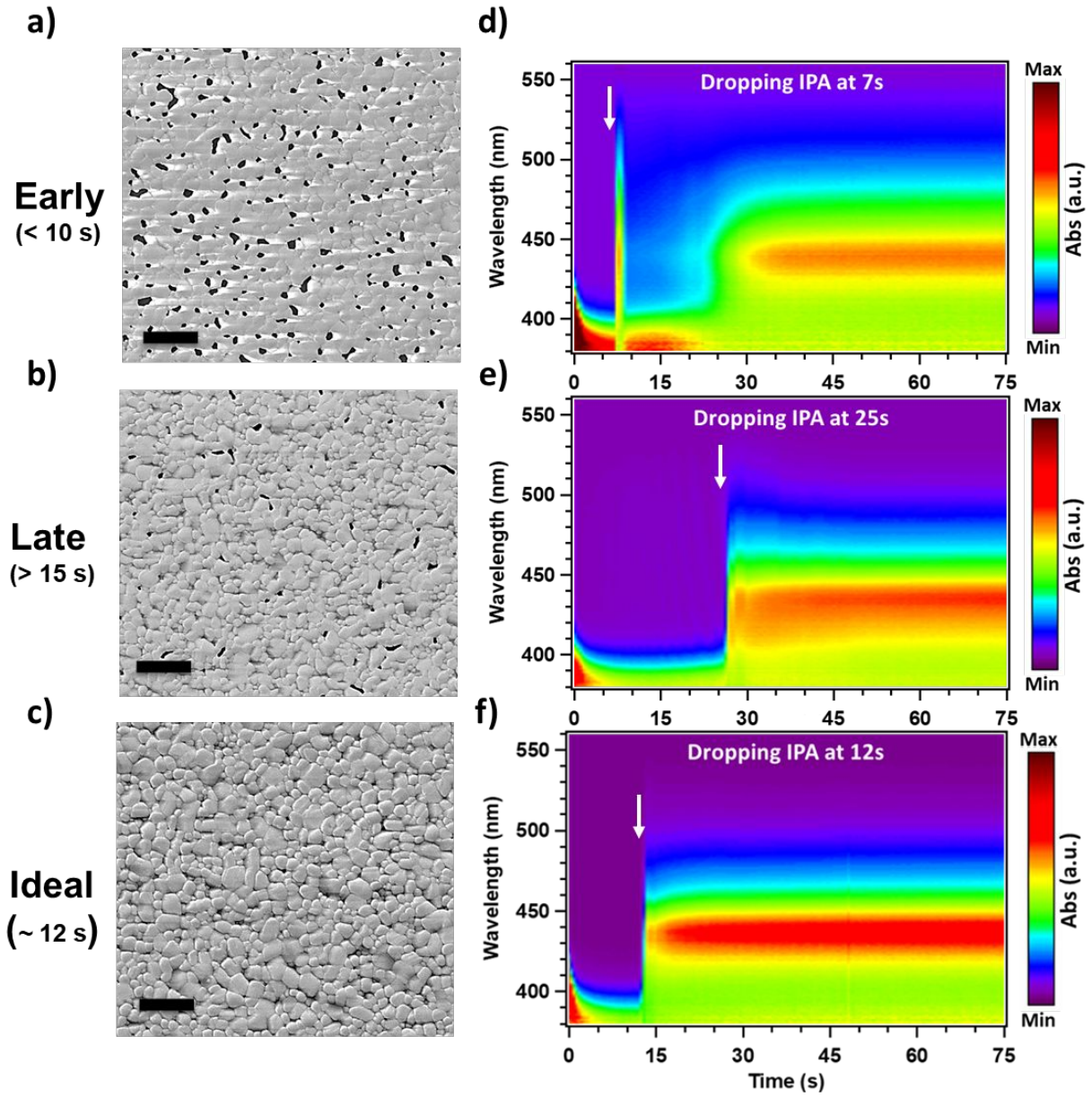

Figure 4 (a-c) SEM images of $Cs_2AgBiBr_6$ thin films prepared with dropping the antisolvent IPA at different dropping times; (a) at 7 s, (b) at 25 s, and (c) at 12 s from the starting of spin-coating. All films in (a-c) were prepared using hot-casting. (d-f) 2D color plots of *in situ* absorption measurements during spin coating of $Cs_2AgBiBr_6$ precursor solution with dropping the antisolvent IPA at different dropping times; (d) at 7 s, (e) at 25 s, and (f) at 12 s from the starting of spin-coating. The time for dropping IPA is marked by a white arrow in (d-f). The scale bar is 2 µm for samples in (a-c).

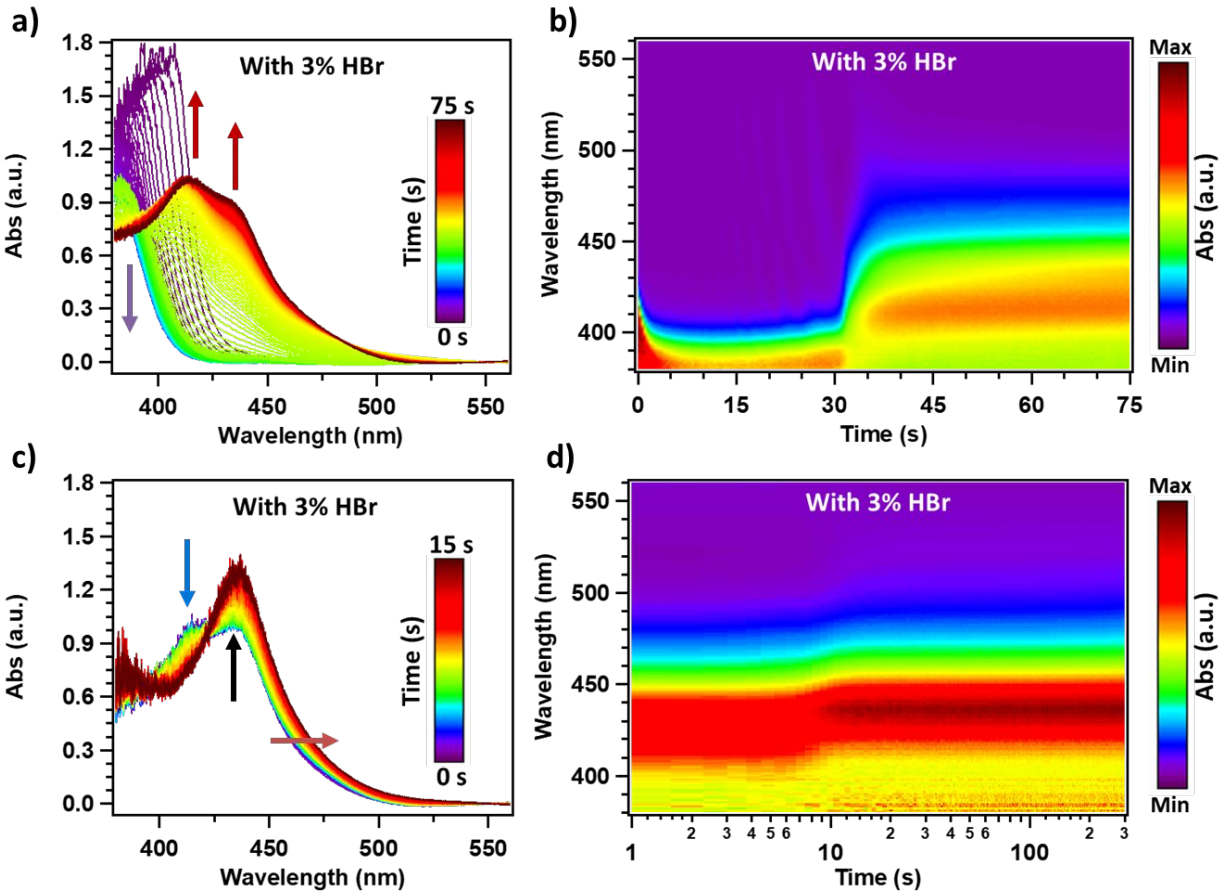

Figure 5 (a&c) Time-resolved absorbance spectra of additive-processing of $Cs_2AgBiBr_6$ using the addition of 3% HBr to precursor solution: (a) during spin coating and (c) during the subsequent thermal annealing. (b) and (d) 2D color plots of in situ absorption measurements for the experiments shown in (a) and (c) respectively.

3. 4. In situ GIWAXS during spin coating and thermal annealing

To investigate the effects of processing on crystallization dynamics during spin coating and thermal annealing, we have performed *in situ* GIWAXS. False-color plots of in situ GIWAXS and time evolution of the (004) scattering peak during spin coating of $Cs_2AgBiBr_6$ are shown in **Figure 6** and **Figure S7**. For the reference sample, only broad scattering from 1.2 $Å^{-1}$ to 2.2 $Å^{-1}$ is observed during the initial steps of spin coating (i.e. solution ejection and solvent evaporation). Upon reaching supersaturation, nucleation and growth of $Cs_2AgBiBr_6$ crystals occur as revealed by the appearance of $Cs_2AgBiBr_6$ diffraction peaks (see **Figure 6**a). The onset of crystallization occurs after ~ 26 s from the start of spin coating (see the evolution of scattering intensity of the (004)

peak in **Figure S7**). For samples prepared with dropping IPA, supersaturation and crystallization occur immediately upon dropping IPA as observed by the emergence of $Cs_2AgBiBr_6$ diffraction peaks (**Figure 6**b). For samples prepared with HBr, we observe a short delay in the onset of crystallization which occurs after ~ 28 s from the start of spin coating (**Figure 6**c and **Figure S7**). This observation of delayed crystallization for HBr-samples matches with the in-situ UV-Vis absorption results as discussed previously (**Figure 3** and **Figure 5**). Nevertheless, no crystalline secondary phases were observed for HBr-samples, unlike the in-situ UV-Vis absorption results that showed an additional phase which we attribute to HBr-complexes. Possibly, these HBr-precursor complexes are amorphous due to the absence of any extra diffraction peaks in the GIWAXS data (**Figure 6**c and **Figure S9**) for the as-cast samples prepared with HBr. This is also supported by the lack of any additional features in their Raman spectra (**Figure S1**) other than $Cs_2AgBiBr_6$ phase. In all cases for as-cast films, we observe diffraction from the $Cs_2AgBiBr_6$ perovskite phase only with no detectable scattering from any crystalline secondary phases as illustrated by the integrated scattering intensity versus q as shown in **Figures S9** and **S10**. It is worth noting that there are slight differences in the onset of $Cs_2AgBiBr_6$ film formation measured by in-situ GIWAXS and in-situ UV-vis absorption spectroscopy but the overall trend is similar. This can be due to differences in the environment of the in situ GIWAXS and in situ UV-Vis absorption measurements (i.e. at the beamline *vs* in the glovebox).

False-color plots of in situ GIWAXS and time evolution of the (004) scattering peak during thermal annealing of spin-coated $Cs_2AgBiBr_6$ thin films are shown in **Figure 7** and **Figure S8**. Upon thermal annealing, we observe an increase in the scattering intensity of the $Cs_2AgBiBr_6$ diffraction peaks indicating an improvement in crystallinity. Hence, the as-cast films likely consist of seeds of $Cs_2AgBiBr_6$ perovskite phase and an amorphous complex phase, while thermal annealing leads to growth of the $Cs_2AgBiBr_6$ perovskite phase at the expense of the amorphous complex phase. Notably, the broad peaks centered around ~ 1.57, 1.73, and 1.89 $Å^{-1}$ correspond to scattering from the PEEK dome (used for the enclosure to create an inert chamber), see **Figures S9** and **S11** which includes a GIWAXS measurement of the bare glass substrate.

During heating from RT to 285 ^{o}C, the scattering intensity remains constant till a threshold temperature is reached at which the scattering intensity starts to increase, see the evolution of

the (004) scattering peak in **Figure 7**b. Such threshold temperatures (marked by arrows in **Figure 7**b) depend on the solvent engineering strategy hinting that the as-cast films possibly have initially either different microstructure and/or different precursor complexes induced by different processing treatments. For the reference sample, we observed a sharp increase in the scattering intensity of the (004) peak upon reaching a heating temperature of ~ 160 ^{o}C. This can possibly be attributed to crystallization of $Cs_2AgBiBr_6$ perovskite phase from amorphous DMSO-precursor complexes. For samples prepared with dropping IPA, the sharp increase occurs earlier upon reaching a heating temperature of ~ 140 ^{o}C. As revealed by thickness measurements (see **Table S1**), the samples prepared with dropping IPA have less retained volatiles (i.e. DMSO) in the as-cast film, perhaps leading to a reduction in the temperature required for crystallization. For samples prepared with HBr, the increase in scattering intensity of the (004) peak starts ~ 120 ^{o}C and develops with a slower rate, then a sharp increase in scattering intensity occurs at ~160 ^{o}C. We hypothesize that the initial crystallization step for samples prepared with HBr can be attributed to the crystallization from HBr-precursor complexes, while the second crystallization step can be attributed to crystallization from DMSO-precursor amorphous complexes. For both samples prepared with IPA or HBr, we observe an additional crystallization step with slower rate after the sharp crystallization step. On the other hand, the reference sample reaches saturation upon the sharp crystallization step.

2D GIWAXS images of the as cast and annealed films measured during in situ annealing are shown in **Figure S10**a-f. The scattering peaks of $Cs_2AgBiBr_6$ crystals appear as isotropic scattering rings indicating homogenous crystallization. This observation can be attributed to crystallization from mainly amorphous phase (with no preferred orientation for crystal growth). Notably, homogeneous nucleation becomes often dominant if it occurs in the interior of an amorphous phase.[52,53] To confirm that the samples prepared at the beamline during in situ measurements have similar microstructure as samples prepared in glovebox, we have measured GIWAXS of samples prepared in glovebox, shown in **Figure S10**g-i. The GIWAXS patterns of samples prepared in glovebox appears very similar to these prepared at the beamline confirming that they have similar crystal structure, compare **Figure S10**d-f and **Figure S10**g-i.

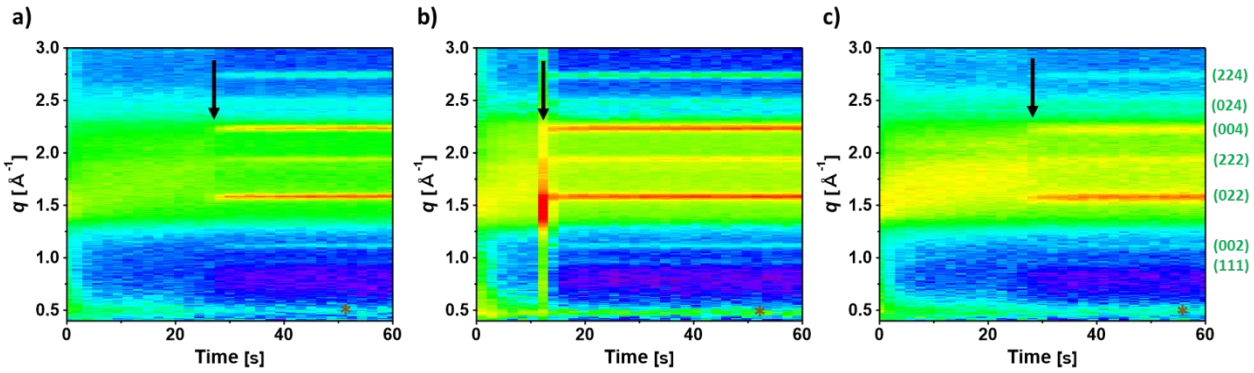

Figure 6 False-color plots of in situ GIWAXS during spin-coating of $Cs_2AgBiBr_6$; (a) prepared without solution engineering (reference sample), (b) with dropping IPA at 12 s from the start of spin coating, and (c) with adding 3% vol HBr to the precursor solution. The onset of crystallization is marked by black arrows. The scattering near ~ 0.5 $Å^{-1}$ (marked as asterisks) is due artifacts.

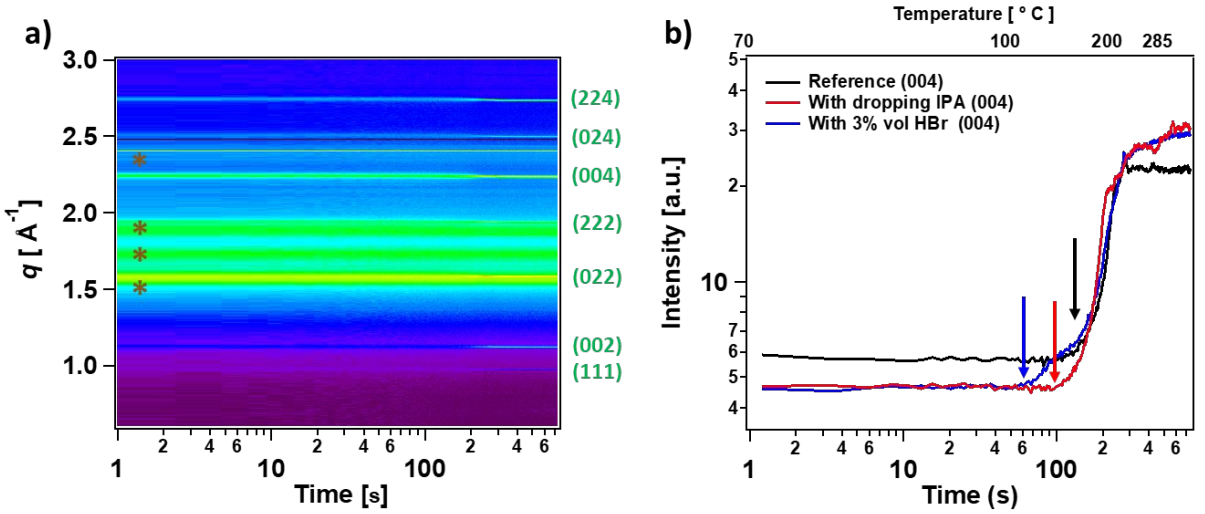

Figure 7 (a) False-color plot of in situ GIWAXS during thermal annealing of spin-coated $Cs_2AgBiBr_6$ thin films prepared without solution engineering (reference sample). (b) Time evolution of the scattering intensities at selected q-value corresponding to the (004) scattering peak; the spin-coated films were prepared without adding HBr or dropping IPA (reference, black line), with dropping IPA at 12 s from the start of spin coating (red line), and with adding HBr to precursor solution (blue line). The $Cs_2AgBiBr_6$ perovskite peaks are labeled on the right of **Figure 7**a. The onset of crystallization is marked in **Figure 7**b by arrows with the same corresponding color as figure curves. The scattering from the PEEK dome gives rise to the broad peaks centered around ~ 1.57, 1.73, 1.89 and 2.4 $Å^{-1}$ (marked as asterisks).

3. 5. Summary of the film formation mechanisms

Based on the above presented results we propose the following explanation of the observed solution engineering effects (antisolvent and additive-assisted synthesis) on the film formation of $Cs_2AgBiBr_6$ (illustrated in **Figure 8**). For all synthesis conditions, the as-cast films are predominantly amorphous with seeds of $Cs_2AgBiBr_6$ crystals as indicated by GIWAXS. The amorphous phase is likely different for the different solution engineering approaches and is speculated to include DMSO-precursor complexes. DLS measurements show that the addition of HBr to the precursor solution has effects on the colloidal formation in solution giving rise to the formation of smaller colloids with narrower distribution of their sizes. During spin coating, HBr induces the formation of an additional phase (possibly HBr-related precursor complexes) besides the amorphous DMSO-precursor and $Cs_2AgBiBr_6$ crystalline phase (**Figure 8**c). Notably, the amount of retained volatiles (HBr and DMSO) in the as-cast films prepared with HBr is similar to the reference samples. However, we hypothesize that the HBr-related precursor complexes are less stable than in the reference sample and therefore, the activation energy for crystallization is reduced as evidenced by the lower crystallization onset temperature (**Figure 7**b).

In situ GIWAXS clearly shows that thermal annealing facilitates the evaporation of volatiles and the growth of $Cs_2AgBiBr_6$ crystals at the expense of the amorphous phases. It was found by in situ GIWAXS and absorbance that the solution engineering treatments have additional effects on the crystallization pathways during spin coating and subsequent thermal annealing. Dropping antisolvent induces immediate crystallization during spin coating and reduces the amount of retained volatiles (i.e., DMSO) in the as-cast films most efficiently. We hypothesize that the reduction of retained DMSO in the as-cast film (**Figure 8**b and **Table S1**) leads to a reduction in the activation energy for the crystallization during thermal annealing as evidenced by the reduced crystallization onset temperature (**Figure 7**b). Previous works have ascribed pinholes in perovskite films to film shrinkage during retained solvent evaporation.[54,55] The higher the retained solvents, the higher the possibility for pinhole formation. There is however an optimum amount of retained volatiles in the film that leads to desirable morphology.[48] Dropping the antisolvent too early leads to a disruption of solution ejection and thinning of the wet film leading to pinholes. Films appear rough and non-homogeneous, see SEM image in **Figure 4**a. Dropping

the antisolvent too late possibly removes most volatiles in the as-cast film making the antisolvent treatment less effective in avoiding the formation of pinholes due to impeded re-arrangement in the film. One drawback however, for the antisolvent treatment is the narrow time window for dropping the antisolvent. Furthermore, this narrow time window is highly affected by the synthesis conditions including the spin coating speed, the solvent choice, and solution concentration, leading to a different critical dropping time for different chemistries and coating conditions. HBr has a positive effect on the precursor solution and film processing resulting in more facile fabrication of pinhole-free $Cs_2AgBiBr_6$ films, and in particular without the need for hot-casting. Furthermore, pinhole-free $Cs_2AgBiBr_6$ films can be obtained from HBr-containing precursor solutions aged for a day without stirring or heating.

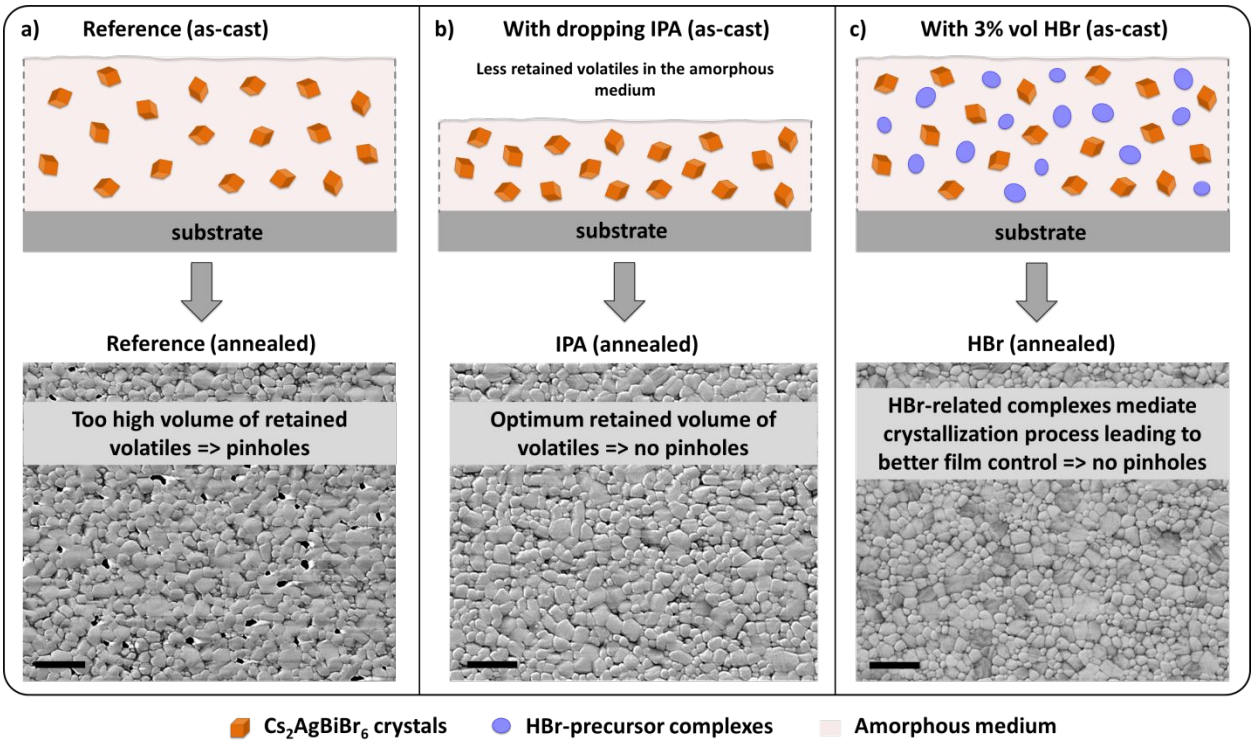

Figure 8 Schematic representation of the as-cast $Cs_2AgBiBr_6$ thin films and SEM images of $Cs_2AgBiBr_6$ annealed films; (a) reference sample, (b) prepared with dropping IPA during spin coating, and (c) prepared with the addition of HBr to precursor solution. The scale bar for samples shown in (a-c) is 2 µm.

4. Conclusion

In conclusion, we have shown the effects of different solution engineering approaches, including antisolvent- and additive (HBr)-assisted synthesis, on the film formation and microstructure of $Cs_2AgBiBr_6$. For films prepared by antisolvent dropping, the antisolvents induce immediate supersaturation and crystallization of the wet film, whereas the dropping time has been shown to be critical in improving the film microstructure. Moreover, the antisolvent dropping was found to reduce the amount of retained volatiles (DMSO) in the as-cast films and facilitates the crystallization during thermal annealing. Nevertheless, we have shown that there is a narrow window for the antisolvent treatment to obtain pinhole-free films. Furthermore, antisolvent dropping requires applying hot casting to be effective in obtaining pinhole-free films. For additive-assisted synthesis, the addition of HBr has been shown to affect the colloid formation in solution by reducing the average size of colloids and making their distribution narrower, perhaps acting as a solubilizing agent of metal halides used in the precursor. This finding agrees with previously reported effects of hydrohalic acids on the colloids in Pb-based perovskite precursor solutions.[51] The addition of HBr to the precursor solution delays the film formation during spin coating, leading to the formation of an additional phase in the as-cast film, and facilitates crystallization during the subsequent thermal annealing, possibly by reducing the activation barrier for crystallization from HBr-containing complexes. Importantly, additive-assisted synthesis has been shown to be effective in obtaining pinhole-free films even with higher final film thickness, and without the need for hot casting. Hence, additive-assisted synthesis appears to be more advantageous than antisolvent treatment in terms of ease of processability of a wide range of film thicknesses. Our results provide a better understanding of the mechanisms of solvent-engineering approaches applied to halide double perovskites and can further guide the development of strategies to control and enhance film formation.

5. Acknowledgements:

This work was funded by the U.S. Department of Energy (DOE), Office of Science, Office of Basic Energy Sciences, Materials Sciences and Engineering Division under Contract No. DE-AC02-05-CH11231 (D2S2 program KCD2S2). Work at the Molecular Foundry was supported by the Office of Science, Office of Basic

Energy Sciences, of the U.S. DOE under Contract No. DE-AC02-05CH11231. This work used beamline 12.3.2 at the Advanced Light Source (ALS), which is a DOE User Facility under Contract No. DE-AC02-05CH11231.

6. References

1 X. Yang, W. Wang, R. Ran, W. Zhou and Z. Shao, *Energy Fuels*, 2020, **34**, 10513–10528.
2 P. Hou, W. Yang, N. Wan, Z. Fang, J. Zheng, M. Shang, D. Fu, Z. Yang and W. Yang, *J. Mater. Chem. C*, 2021, **9**, 9659–9669.
3 H. Lei, D. Hardy and F. Gao, *Adv. Funct. Mater.*, 2021, **31**, 2105898.
4 J. Y. Kim, J.-W. Lee, H. S. Jung, H. Shin and N.-G. Park, *Chem. Rev.*, 2020, **120**, 7867–7918.
5 F. Giustino and H. J. Snaith, *ACS Energy Lett.*, 2016, **1**, 1233–1240.
6 S. Sun, N. T. P. Hartono, Z. D. Ren, F. Oviedo, A. M. Buscemi, M. Layurova, D. X. Chen, T. Ogunfunmi, J. Thapa, S. Ramasamy, C. Settens, B. L. DeCost, A. G. Kusne, Z. Liu, S. I. P. Tian, I. M. Peters, J. P. Correa-Baena and T. Buonassisi, *Joule*, 2019, **3**, 1437–1451.
7 M. Usman and Q. Yan, *Crystals*, 2020, **10**, 62.
8 Y. Zhao, K. Cruse, M. Abdelsamie, G. Ceder and C. M. Sutter-Fella, *Matter*, 2021, **4**, 1801–1831.
9 A. H. Slavney, T. Hu, A. M. Lindenberg and H. I. Karunadasa, *J. Am. Chem. Soc.*, 2016, **138**, 2138–2141.
10 T. T. Tran, J. R. Panella, J. R. Chamorro, J. R. Morey and T. M. McQueen, *Mater. Horiz.*, 2017, **4**, 688–693.
11 E. T. McClure, M. R. Ball, W. Windl and P. M. Woodward, *Chem. Mater.*, 2016, **28**, 1348–1354.
12 M. R. Filip, S. Hillman, A. A. Haghighirad, H. J. Snaith and F. Giustino, *J. Phys. Chem. Lett.*, 2016, **7**, 2579–2585.
13 K. Z. Du, W. Meng, X. Wang, Y. Yan and D. B. Mitzi, *Angew. Chem. - Int. Ed.*, 2017, **56**, 8158–8162.
14 E. Greul, M. L. Petrus, A. Binek, P. Docampo and T. Bein, *J. Mater. Chem. A*, 2017, **5**, 19972–19981.
15 W. A. Dunlap-Shohl, Y. Zhou, N. P. Padture and D. B. Mitzi, *Chem. Rev.*, 2019, **119**, 3193–3295.
16 Q. Han, Y. Bai, J. Liu, K. Du, T. Li, D. Ji, Y. Zhou, C. Cao, D. Shin, J. Ding, A. D. Franklin, J. T. Glass, J. Hu, M. J. Therien, J. Liu and D. B. Mitzi, *Energy Environ. Sci.*, 2017, **10**, 2365–2371.
17 Y. Sun, J. Peng, Y. Chen, Y. Yao and Z. Liang, *Sci. Rep.*, 2017, **7**, 46193.
18 T. Li, Y. Pan, Z. Wang, Y. Xia, Y. Chen and W. Huang, *J. Mater. Chem. A*, 2017, **5**, 12602–12652.
19 S. Liu, Y. Guan, Y. Sheng, Y. Hu, Y. Rong, A. Mei and H. Han, *Adv. Energy Mater.*, 2020, **10**, 1902492.
20 M. Abdelsamie, T. Li, F. Babbe, J. Xu, Q. Han, V. Blum, C. M. Sutter-Fella, M. David B. and M. F. Toney, *ACS Appl. Mater. Interfaces*.
21 N. J. Jeon, J. H. Noh, Y. C. Kim, W. S. Yang, S. Ryu and S. I. Seok, *Nat. Mater.*, 2014, **13**, 897–903.
22 K.-M. Lee, C.-J. Lin, B.-Y. Liou, S.-M. Yu, C.-C. Hsu, V. Suryanarayanan and M.-C. Wu, *Sol. Energy Mater. Sol. Cells*, 2017, **172**, 368–375.
23 M. Qin, K. Tse, T.-K. Lau, Y. Li, C.-J. Su, G. Yang, J. Chen, J. Zhu, U.-S. Jeng, G. Li, H. Chen and X. Lu, *Adv. Mater.*, 2019, **31**, 1901284.
24 M. Abdelsamie, J. Xu, K. Bruening, C. J. Tassone, H.-G. Steinrück and M. F. Toney, *Adv. Funct. Mater.*, 2020, **30**, 2001752.
25 R. Szostak, P. E. Marchezi, A. dos S. Marques, J. C. da Silva, M. S. de Holanda, M. M. Soares, H. C. N. Tolentino and A. F. Nogueira, *Sustain. Energy Fuels*, 2019, **3**, 2287–2297.
26 R. Munir, A. D. Sheikh, M. Abdelsamie, H. Hu, L. Yu, K. Zhao, T. Kim, O. El Tall, R. Li, D.-M. Smilgies and A. Amassian, *Adv. Mater.*, 2017, **29**, 1604113.
27 Q. Hu, L. Zhao, J. Wu, K. Gao, D. Luo, Y. Jiang, Z. Zhang, C. Zhu, E. Schaible, A. Hexemer, C. Wang, Y. Liu, W. Zhang, M. Grätzel, F. Liu, T. P. Russell, R. Zhu and Q. Gong, *Nat. Commun.*, 2017, **8**, 1–9.
28 T. Bin Song, Z. Yuan, M. Mori, F. Motiwala, G. Segev, E. Masquelier, C. V. Stan, J. L. Slack, N. Tamura and C. M. Sutter-Fella, *Adv. Funct. Mater.*, 2019, **1908337**, 1–11.

29 C. M. Sutter-Fella, *Adv. Energy Mater.*, 2021, **11**, 2003534.
30 O. Kononova, H. Huo, T. He, Z. Rong, T. Botari, W. Sun, V. Tshitoyan and G. Ceder, *Sci. Data*, 2019, **6**, 203.
31 L. Weston, V. Tshitoyan, J. Dagdelen, O. Kononova, A. Trewartha, K. A. Persson, G. Ceder and A. Jain, *J. Chem. Inf. Model.*, 2019, **59**, 3692–3702.
32 T. He, W. Sun, H. Huo, O. Kononova, Z. Rong, V. Tshitoyan, T. Botari and G. Ceder, *Chem. Mater.*, 2020, **32**, 7861–7873.
33 S. P. Ong, W. D. Richards, A. Jain, G. Hautier, M. Kocher, S. Cholia, D. Gunter, V. L. Chevrier, K. A. Persson and G. Ceder, *Comput. Mater. Sci.*, 2013, **68**, 314–319.
34 M. Abdelsamie, K. Zhao, M. R. Niazi, K. W. Chou and A. Amassian, *J. Mater. Chem. C*, 2014, **2**, 3373–3381.
35 K. Wang, R.-Z. Liang, J. Wolf, Q. Saleem, M. Babics, P. Wucher, M. Abdelsamie, A. Amassian, M. R. Hansen and P. M. Beaujuge, *Adv. Funct. Mater.*, 2016, **26**, 7103–7114.
36 Y. Yao, S.-W. Zhang, Z. Liu, C.-Y. Wang, P. Liu, L. Ma, G. Wei and F. Kang, *RSC Adv.*, 2021, **11**, 26415–26420.
37 Y. Liu, A. Nag, L. Manna and Z. Xia, *Angew. Chem. Int. Ed.*, 2021, **60**, 11592–11603.
38 L. Li, H. Shao, X. Wu, W. Chen, J. Zhu, B. Dong, L. Xu, W. Xu, J. Hu, M. Zhou, Y. Ji, H. Song and X. Bai, *Mater. Res. Bull.*, 2022, **147**, 111645.
39 F. Locardi, M. Cirignano, D. Baranov, Z. Dang, M. Prato, F. Drago, M. Ferretti, V. Pinchetti, M. Fanciulli, S. Brovelli, L. De Trizio and L. Manna, *J. Am. Chem. Soc.*, 2018, **140**, 12989–12995.
40 E. López-Fraguas, S. Masi and I. Mora-Seró, *ACS Appl. Energy Mater.*, 2019, **2**, 8381–8387.
41 C.-F. Lai, Y.-C. Chang and Y.-C. Tien, *ACS Appl. Nano Mater.*, , DOI:10.1021/acsanm.0c03273.
42 R. Zeng, L. Zhang, Y. Xue, B. Ke, Z. Zhao, D. Huang, Q. Wei, W. Zhou and B. Zou, *J. Phys. Chem. Lett.*, 2020, **11**, 2053–2061.
43 J. C. Dahl, W. T. Osowiecki, Y. Cai, J. K. Swabeck, Y. Bekenstein, M. Asta, E. M. Chan and A. P. Alivisatos, *Chem. Mater.*, 2019, **31**, 3134–3143.
44 H. Zheng, Z. Tang, P. Liang, H. Shu, L. Wang, J. Huang, A. A. Levin, P. N. Brunkov and Z. Liu, *Thin Solid Films*, 2021, **732**, 138781.
45 R. Ahmad, G. V. Nutan, D. Singh, G. Gupta, U. Soni, S. Sapra and R. Srivastava, *Nano Res.*, 2021, **14**, 1126–1134.
46 H. Li, X. Shan, J. N. Neu, T. Geske, M. Davis, P. Mao, K. Xiao, T. Siegrist and Z. Yu, *J. Mater. Chem. C*, 2018, **6**, 11961–11967.
47 R. A. Kerner, L. Zhao, Z. Xiao and B. P. Rand, *J. Mater. Chem. A*, 2016, **4**, 8308–8315.
48 T.-B. Song, Z. Yuan, F. Babbe, D. P. Nenon, E. Aydin, S. De Wolf and C. M. Sutter-Fella, *ACS Appl. Energy Mater.*, 2020, **3**, 2386–2393.
49 S. Pratap, F. Babbe, N. S. Barchi, Z. Yuan, T. Luong, Z. Haber, T.-B. Song, J. L. Slack, C. V. Stan, N. Tamura, C. M. Sutter-Fella and P. Müller-Buschbaum, *Nat. Commun.*, 2021, **12**, 5624.
50 W. Gao, C. Ran, J. Xi, B. Jiao, W. Zhang, M. Wu, X. Hou and Z. Wu, *ChemPhysChem*, 2018, **19**, 1696–1700.
51 D. P. McMeekin, Z. Wang, W. Rehman, F. Pulvirenti, J. B. Patel, N. K. Noel, M. B. Johnston, S. R. Marder, L. M. Herz and H. J. Snaith, *Adv. Mater.*, 2017, **29**, 1607039.
52 S. Raoux and T. J. Ibm, in *Advances in Non-volatile Memory and Storage Technology*, ed. Y. Nishi, Woodhead Publishing, 2014, pp. 161–199.
53 L. Yu, M. R. Niazi, G. O. N. Ndjawa, R. Li, A. R. Kirmani, R. Munir, A. H. Balawi, F. Laquai and A. Amassian, *Sci. Adv.*, 2017, **3**, e1602462.
54 D. Gedamu, I. M. Asuo, D. Benetti, M. Basti, I. Ka, S. G. Cloutier, F. Rosei and R. Nechache, *Sci. Rep.*, 2018, **8**, 12885.

55 Z. Yuan, Y. Yang, Z. Wu, S. Bai, W. Xu, T. Song, X. Gao, F. Gao and B. Sun, *ACS Appl. Mater. Interfaces*, 2016, **8**, 34446–34454.